J. Fluid Mech. (2016), *vol.* 806, *pp.* 234–253.
doi:10.1017/jfm.2016.590

Asymptotic analysis for the propagation and arresting process of a finite dry granular mass down a rough incline

K.-L. Lee[1] **and F.-L. Yang**[1,†]

[1]Department of Mechanical Engineering, National Taiwan University, Taipei 10617, Taiwan

(Received 17 November 2014; revised 27 July 2016; accepted 3 September 2016;
first published online 30 September 2016)

This work presents an asymptotic analysis for the propagation and arresting process of a two-dimensional finite granular mass down a rough incline in a shallow configuration. Bulk shear stress and arresting mechanism are formulated according to the coherence length model that considers momentum transport at a length scale over which grains are spatially correlated. A Bagnold-like streamwise velocity and a non-zero transverse velocity are solved and integrated into a surface kinematic condition to give an advection–diffusion equation for the bulk surface profile, $h(x, t)$, that is solved using the matched asymptotic method. These flow solutions are further employed to determine composite solutions for a flow-front trajectory and a local coherence length, $l(x, t)$, which reveals smooth growth of $h(x, t)$ and $l(x, t)$ from zero at the propagating front with $l(x, t) \ll h(x, t)$. At the rear, $h(x, t)$ vanishes but $l(x, t)$ asymptotes to a constant that depends on inclination angle. According to the arresting mechanism, the location where $l(x, t) \sim h(x, t)$ is solved to the leading order to locate the deposition front so that its propagation dynamics can be derived. A finite flow arrest time, T_d, and the corresponding finite run-out distance, L_d, are evaluated when all the flowing mass has passed the deposition front and are employed to construct a modified front trajectory with the deposition effect. The predicted run-out distance and front trajectory profile compare reasonably well with experimental data in the literature on inclinations at angles higher than the material repose angle.

Key words: geophysical and geological flows, granular media, shallow water flows

1. Introduction

Dry granular flows down a solid surface at an inclination angle θ have been extensively studied due to their frequent appearance in industrial processes, geophysical events and rheology tests. Under the action of gravity, constituent grains move towards the base into a dense configuration with multiple enduring contacts so that the flow is often dense and frictional in nature. For a continuous steady dense flow of uniform thickness, experiments and numerical simulations have revealed a minimum flow depth, h_{stop}, below which the flow stops *en masse*. This critical thickness is a function of θ, $h_{stop}(\theta)$, that diverges at a lower threshold, θ_1, and diminishes

†Email address for correspondence: fulingyang@ntu.edu.tw

monotonically to zero at an upper limit, θ_2 (Daerr & Douady 1999; Pouliquen 1999; Silbert, Landry & Grest 2003; GDRMidi 2004; Borzsonyi, Halsey & Ecke 2008; Staron 2008). These findings suggest a complex rheological behaviour regarding the manner in which a moving bulk halts upon changes of flow condition. On the other hand, the motion of a finite granular mass is often unsteady, non-uniform and exhibits a finite run-out distance and flow arrest time. For example, Pouliquen & Forterre (2002) released finite glass beads down a roughened bed and observed a flow-to-no-flow arresting transition that first developed at the rear and moved towards the front so that the whole bulk formed a solid deposit in a certain period. Similar to most gravity-driven flows, granular incline flows often propagate in a shallow configuration and the small height-to-length aspect ratio can be exploited together with the dense nature of the flow to simplify the conservation equations of mass and momentum into an incompressible shallow flow model. The resulting equations govern the flow depth and depth-averaged streamwise velocity with a phenomenological model for basal friction (Savage & Hutter 1989; Daerr 2001; Pouliquen & Forterre 2002; Hogg 2007). In addition, the influence of fluid-to-solid transition on bulk dynamics has also been accounted for by incorporating a deposition scheme in terms of flow depth and internal friction angle (Bouchaud *et al.* 1994), or with further dependence on transition interface velocity (Boutreux, Raphael & de Gennes 1998; Tai & Kuo 2008; Gray & Ancey 2009). Owing to the flow-dependent basal friction and deposition scheme, a numerical solution is often required and has been shown to reproduce many flow features observed in laboratory experiments of an inclined flows (Mangeney-Castelnau *et al.* 2010) or flows due to a column collapse (Balmforth & Kerswell 2005; Mangeney-Castelnau *et al.* 2005).

Such a feasible simplification via depth averaging, nonetheless, causes information loss in the method for how a fluid–solid interface may develop across a layer during the deposition process, consequently necessitating further modelling efforts. A two-dimensional non-depth-averaged Coulomb–viscoplastic sliding law with pressure and rate dependence has been proposed and integrated to a shallow flow model so that the temporal and spatial evolution of a solid–liquid interface can be numerically solved (Domnik & Pudasaini 2012; Domnik *et al.* 2013). Different theories have also been proposed to address the h_{stop} phenomenon for a continuous steady flow with a uniform thickness. Kinetic theory of a dense gas has been employed to show that solid phase develops when the fluctuation energy generated by particle collisions is insufficient to compensate for the energy dissipated due to inelastic or frictional contact (Louge 2003; Jenkins 2006; Kumaran 2008). In the non-local self-activation theory (Pouliquen & Forterre 2009), a flow coming to a halt is explained by grain-level local avalanche events in a thin layer being too rare to self-trigger a continuous flow. Another class of models based on the Ginzburg–Landau phase transition theory, which introduces an order parameter to describe the extent of fluidization of a bulk, can also reproduce the h_{stop} phenomenon (Aranson & Tsimring 2002; Kamrin & Henann 2015).

Nonetheless, it is noted that the h_{stop} phenomenon is first captured by the coherence length model developed by Ertas & Halsey (2002) considering how bulk dynamics depends on the spatial correlation between grains over a length scale of l owing to their multiple enduring contacts. This coherence length l should evolve with the flow and the authors match the time scale of growth by inelastic interaction between grains, $(l|\partial_y u|/g)f(e)$, to that of destruction, $(l|\partial_{yy} u|)^{-1}$, when the motions of those spatially

correlated grains are no longer compatible with bulk shear. A dynamic equation for l is then formulated as

$$l^2 \left| \frac{\partial}{\partial y} \left[\left(\frac{\partial u}{\partial y} \right)^2 \right] \right| = \hat{a} g f(e), \tag{1.1}$$

where $u(y)$ is the downslope velocity profile, with y measuring the perpendicular distance to the base, g represents gravity, $f(e) = (1 - e)/e$ is a proposed function that decreases monotonically with the grain coefficient of restitution, e, and $\hat{a}$ is a constant of order unity. When l is sufficiently smaller than the flow height, momentum transport across a viscous transport length l_v, which is associated with l, during a shear time $(\partial_y u)^{-1}$ can result in a stress as

$$\tau = \rho l_v^2 \left(\frac{\partial u}{\partial y} \right)^2. \tag{1.2}$$

This is formulated following the concept of how eddy-induced stress in turbulent flows is modelled in Prandtl's mixing-length theory. Since the viscous transport length should approach a grain diameter D to recover the Bagnold stress $\rho D^2 (\partial_y u)^2$ (Bagnold 1954) in the rapid collisional regime where the correlation between grains diminishes, Ertas & Halsey (2002) proposed the following asymptotic relation:

$$l_v^2 = l^2 \left(1 + \hat{b} \frac{D}{l} + \cdots \right), \tag{1.3}$$

where $\hat{b}$ represents a constant accounting for the first-order correction of such a finite-size effect. Although this constitutive relation is developed via scaling arguments, Ertas & Halsey (2002) demonstrated that its application to steady uniform-thickness flows can qualitatively capture the Bagnold velocity profile (GDRMidi 2004) and Pouliquen's flow rule (Pouliquen 1999). In particular, the coherence length is solved to be $l \sim D/[\sin\theta - \sin\theta_r(e)]$, which qualitatively captures the monotonically increasing $h_{stop}(\theta)$ when $l(\theta)$ in a decelerating bulk approaches the flow thickness as θ is diminished towards the predicted repose angle $\theta_r(e) = \sin^{-1}[\hat{a} f(e)]$ corresponding to the measured angle θ_1 (Ertas & Halsey 2002). The speculated correspondence between h_{stop} and spatially correlated grain motions has been evidenced in experiments (Pouliquen 2004) and numerical simulations (Baran *et al.* 2006; Staron 2008). Even more encouraging, the concept of coherence length has also been integrated with the well-accepted $\mu(I)$ constitutive relation for shear stress for a gentle slope with smooth particles so that the $h_{stop}(\theta)$ function can be analytically solved for steady uniform flows by simply replacing τ in (1.2) (GDRMidi 2004).

Hence, this work attempts to apply the coherence length model for the propagation of finite granular mass down a straight rough incline to examine whether the finite run-out distance and arrest time can be captured. This will test if the fluid-to-solid transition across the layer can be effectively inferred by the associated arresting mechanism, which is the primary objective of this work. The second aim is to formulate a theoretical framework on which analytical solutions may be sought to complement the findings from experiments and the numerical solution to a depth-averaged shallow layer model. We focus on the dynamics of a shallow layer in the long run-out down a mild incline so that the influences of initial condition and bulk inertia may be negligible and the small aspect ratio permits asymptotic solutions. The governing equations are formulated in § 2 and the asymptotic flow solutions are

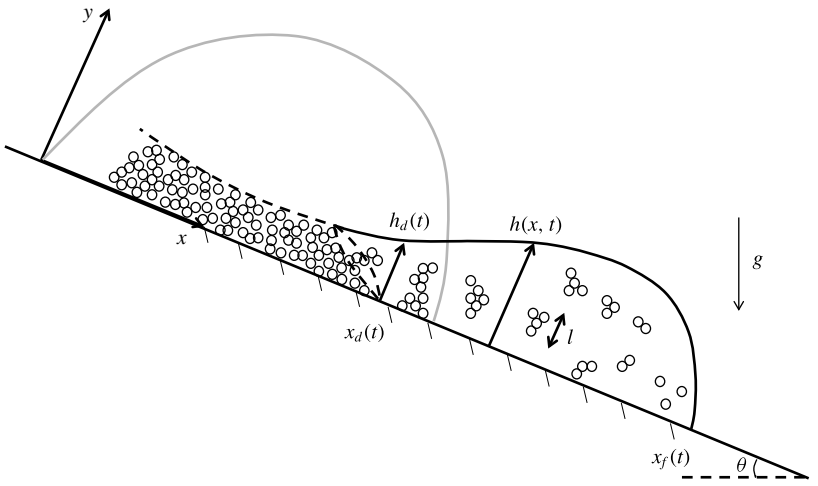

FIGURE 1. Illustration and nomenclature of the problem. The black solid and dashed lines depict possible surface profiles of the flow and solid deposit, while an initial packing is shown by the grey solid line. The symbol $h(x, t)$ represents the instantaneous flow surface, $x_f(t)$ the location of the flow front, and $x_d(t)$ and $h_d(t)$ represent the location and surface height at the deposit front, respectively. The local coherence length among spatially correlated grains is l. An undetermined solid–liquid interface depth profile is presented by both the concave and convex dashed lines.

derived in § 3 at a fully flowing state (with $l \ll h$) and exploited to estimate how l grows in the flow. A dynamic model is developed to describe how the front of a solid deposition wave propagates downstream in § 4, which is further modified to correct the errors in assuming that the propagation dynamics is decoupled from the deposition process. The final model is then evaluated by comparing the predictions of a transient front trajectory at $\theta = 23^\circ$ and the final run-out distances on different slopes to those measured by Pouliquen & Forterre (2002). Finally, a summary and discussions on the limitations of the current analysis are given in § 5.

2. Governing equations

2.1. *Problem description*

Consider a two-dimensional granular material of total mass M being released down a rough incline at a mild angle θ from the horizontal as shown in figure 1. A Cartesian coordinate system Oxy is defined at the rear end of the mass upon initiation, with x and y being the downslope and the slope-normal coordinates, respectively. The corresponding velocity components are $u(x, y, t)$ and $v(x, y, t)$, the free-surface profile normal to the base is $h(x, t)$, and the location of the flow front is $x_f(t)$. From experimental observations, a static deposit may form in the rear and a flow-to-no-flow transition occurs midstream to create a fluid–solid interface that moves downstream. When the interface eventually reaches the flow front, the entire mass stops at finite run-out distance of L_d and arrest time T_d (Pouliquen & Forterre 2002). Here, we use the coherence length model developed by Ertas & Halsey (2002) and their arresting mechanism to determine if these observed flow features may be reproduced analytically.

2.2. *Model formulation*

When the flow coherence length is sufficiently small, bulk motion may be approximated by a shallow, isotropic and incompressible flow with a constant bulk density ρ (Pudasaini & Hutter 2007; Andreotti, Forterre & Pouliquen 2013). The conservation equations of mass and momentum are

$$\frac{\partial u}{\partial x}+\frac{\partial v}{\partial y}=0, \tag{2.1}$$

$$\rho\left(\frac{\partial u}{\partial t}+u\frac{\partial u}{\partial x}+v\frac{\partial u}{\partial y}\right)=\frac{\partial \sigma_{xx}}{\partial x}+\frac{\partial \sigma_{yx}}{\partial y}+\rho g\sin\theta, \tag{2.2}$$

$$0=\frac{\partial \sigma_{yy}}{\partial y}-\rho g\cos\theta. \tag{2.3}$$

The y-momentum equation in (2.3) has been simplified, under the condition of flow shallowness, into a balance between the gradient of the normal stress component and the y-component of gravity (Pudasaini & Hutter 2007; Andreotti *et al.* 2013). The assumption of flow isotropy gives $\sigma_{xx}=\sigma_{yy}$ and the shear component, σ_{yx}, is described by the coherence length model using (1.1)–(1.3). These governing equations are subject to stress-free and kinematic conditions on the free surface,

$$\sigma_{xx}=\sigma_{yy}=\sigma_{yx}=0, \quad \text{at } y=h(x,t), \tag{2.4}$$

$$\frac{\partial h}{\partial t}+u\frac{\partial h}{\partial x}-v=0, \quad \text{at } y=h(x,t), \tag{2.5}$$

and to no-penetration and no-slip boundary conditions at the base,

$$v=0, \quad \text{at } y=0, \tag{2.6}$$

$$u=0, \quad \text{at } y=0. \tag{2.7}$$

Flow variables are non-dimensionalized by characteristic flow height and length, H and L, downstream flow speed, U, and bulk density, ρ, into

$$\left.\begin{gathered}(x,y,h,x_d,h_d,L_d,l,l_v,D)=L(\tilde{x},\epsilon\tilde{y},\epsilon\tilde{h},\tilde{x}_d,\epsilon\tilde{h}_d,\tilde{L}_d,\epsilon\tilde{l},\epsilon\tilde{l}_v,\epsilon\tilde{D}),\\ (u,v)=U(\tilde{u},\epsilon\tilde{v}),\quad (t,T_d)=(L/U)(\tilde{t},\tilde{T}_d),\quad \sigma_{yx}=\rho U^2\tilde{\sigma}_{yx},\quad M=\rho HL\tilde{M},\end{gathered}\right\} \tag{2.8}$$

with a small flow aspect ratio, $\epsilon\equiv H/L\ll 1$. Flow Froude number, $Fr\equiv U/\sqrt{gH}$, is defined consistently as that used by Ertas & Halsey (2002) on uniform flows and by Pouliquen & Forterre (2002), whose experimental results are adopted later to evaluate our model. We have also worked with the conventional and extended Froude number with reduced gravity, $\sqrt{gH\cos\theta}$ (Borzsonyi *et al.* 2008; Domnik *et al.* 2013; Edwards & Gray 2014), so that the resulting equations and the corresponding asymptotic solutions possess complex coefficients with multiple appearances of $\cos\theta$. Since $\cos\theta$ is of order unity on milder slopes, removing $\cos\theta$ from these coefficients does not change the nature of the equations, which supports the current Fr. The dimensionless continuity and x-momentum equation become

$$\frac{\partial \tilde{u}}{\partial \tilde{x}}+\frac{\partial \tilde{v}}{\partial \tilde{y}}=0, \tag{2.9}$$

$$\epsilon Fr^2\left(\frac{\partial \tilde{u}}{\partial \tilde{t}}+\tilde{u}\frac{\partial \tilde{u}}{\partial \tilde{x}}+\tilde{v}\frac{\partial \tilde{u}}{\partial \tilde{y}}\right)=\epsilon\cos\theta\frac{\partial \tilde{h}}{\partial \tilde{x}}+Fr^2\frac{\partial \tilde{\sigma}_{yx}}{\partial \tilde{y}}+\sin\theta, \tag{2.10}$$

where the normal stress has been obtained from the y-momentum equation to give a hydrostatic profile, $\sigma_{yy}=\sigma_{xx}=\rho g\cos\theta(h-y)$, and applied in (2.10). The corresponding constitutive equations (1.1)–(1.3) become

$$Fr^2\tilde{l}^2\left|\frac{\partial}{\partial\tilde{y}}\left(\frac{\partial\tilde{u}}{\partial\tilde{y}}\right)^2\right|=\hat{a}f(e), \tag{2.11}$$

$$\tilde{\sigma}_{yx}=\tilde{l}_v^2\left(\frac{\partial\tilde{u}}{\partial\tilde{y}}\right)^2, \tag{2.12}$$

$$\tilde{l}_v^2=\tilde{l}^2\left(1+\hat{b}\frac{\tilde{D}}{\tilde{l}}\right). \tag{2.13}$$

The dimensionless dynamic and kinematic boundary conditions from (2.4) to (2.7) are

$$\tilde{\sigma}_{xx}=\tilde{\sigma}_{yy}=\tilde{\sigma}_{yx}=0,\quad \text{at } \tilde{y}=\tilde{h}(\tilde{x},\tilde{t}), \tag{2.14}$$

$$\frac{\partial\tilde{h}}{\partial\tilde{t}}+\tilde{u}\frac{\partial\tilde{h}}{\partial\tilde{x}}-\tilde{v}=0,\quad \text{at } \tilde{y}=\tilde{h}(\tilde{x},\tilde{t}), \tag{2.15}$$

$$\tilde{v}=0,\quad \text{at } \tilde{y}=0, \tag{2.16}$$

$$\tilde{u}=0,\quad \text{at } \tilde{y}=0. \tag{2.17}$$

Note that we have adopted the gravity wave speed, $\sqrt{gH}$, to scale the propagating velocity down mild slopes as in Gray & Edwards (2014), which is different from the fast scale, $\sqrt{gL}$, used by Savage & Hutter (1989) for motions on steep slopes. Limiting to flows with Fr of order unity, the corresponding coherence length scale would also be of order unity by (2.11) so that the essential deposition mechanism can be revealed. As a result, the inertial term in (2.10) scaled by ϵFr^2 becomes negligible when $\epsilon\to 0$. Such a simplification has been justified for the depth-averaged model adopted in Pouliquen & Forterre (2002) where the propagating inertia was reported to drop faster than the other terms shortly after the onset of an avalanche. Although the gradient of normal stress is also scaled by ϵ, it can be a non-negligible mechanism for local momentum balance when $\partial\tilde{h}/\partial\tilde{x}$ is large and hence it is kept. So, for non-inertial and critical ($Fr\sim 1$) flows, (2.10) becomes

$$0\simeq\epsilon\cos\theta\frac{\partial\tilde{h}}{\partial\tilde{x}}+\frac{\partial\tilde{\sigma}_{yx}}{\partial\tilde{y}}+\sin\theta. \tag{2.18}$$

When a flow accelerates on a steep incline with $\theta>\theta_2$, equation (2.18) is no longer valid and the fast velocity scale, $\sqrt{gL}$, should be adopted so that $Fr\sim\epsilon^{-1}$ to preserve the inertial term in the leading-order momentum balance. Based on (2.11), the coherence length scale in such an accelerating flow would be greatly reduced ($\sim\epsilon^2$) so that the arresting mechanism is weak and the bulk propagates downstream without any deposit.

Equations (2.11)–(2.13) and (2.18) with the boundary conditions (2.15) can be solved jointly to determine the coherence length (see appendix A),

$$\tilde{l}=\frac{\sin\theta_r\,\hat{b}\tilde{D}}{F(\theta,\theta_r,\tilde{h})}, \tag{2.19}$$

and the shear rate

$$\frac{\partial\tilde{u}}{\partial\tilde{y}}=\frac{F(\theta,\theta_r,\tilde{h})}{\sqrt{\sin\theta_r}\,\hat{b}\tilde{D}}(\tilde{h}-\tilde{y})^{1/2}, \tag{2.20}$$

with

$$F(\theta, \theta_r, \tilde{h}) = \sin\theta - \epsilon \cos\theta \frac{\partial \tilde{h}}{\partial \tilde{x}} - \sin\theta_r \quad \text{where} \quad \sin\theta_r = \hat{a} f(e). \tag{2.21}$$

The solution of the shear rate from (2.20) is further integrated with the no-slip condition, equation (2.17), to give the following Bagnold-like streamwise velocity profile:

$$\tilde{u} = \frac{2}{3} \frac{F(\theta, \theta_r, \tilde{h})}{\sqrt{\sin\theta_r}\, \hat{b}\tilde{D}} [\tilde{h}^{3/2} - (\tilde{h} - \tilde{y})^{3/2}]. \tag{2.22}$$

The dimensionless continuity equation, equation (2.9), can then be integrated along $\tilde{y}$ with (2.22) to give the velocity component normal to the slope:

$$\tilde{v} = -\frac{2}{3} \frac{\partial}{\partial \tilde{x}} \left\{ \frac{F(\theta, \theta_r, \tilde{h})}{\sqrt{\sin\theta_r}\, \hat{b}\tilde{D}} \left[\tilde{h}^{3/2}\tilde{y} - \frac{2}{5}(\tilde{h} - \tilde{y})^{5/2} - \frac{2}{5}\tilde{h}^{5/2} \right] \right\}. \tag{2.23}$$

The dependence of streamwise velocity and its dependence on $\tilde{h}$ are similar to that derived for steady uniform flows (GDRMidi 2004), but the terms $\partial\tilde{h}/\partial\tilde{x}$ and $\tilde{v}$ are non-zero for the current flow of varying thickness. The factor $F(\theta, \theta_r, \tilde{h})$ in u and v represents the local driving force after the gravity component is balanced by the hydraulic pressure gradient and the inelastic resistance force $\hat{a} f(e)$. For a steady flow of uniform thickness, $\partial\tilde{h}/\partial\tilde{x} = 0$ and $F = 0$ (when $\tilde{u} = 0$) determines $\theta_r = \sin^{-1}[\hat{a} f(e)]$, which should be correlated to the lowest threshold angle θ_1 for a continuous uniform surface flow observed in recovering the experimental phenomenon in Pouliquen (1999), as discussed in § 1. It should be noted that (2.22) and (2.23) and the following analysis are valid only when $F(\theta, \theta_r, \tilde{h}) > 0$; otherwise, a back-flow with negative $\tilde{u}$ and $\tilde{v}$ can occur, for which the current scaling needs re-examination. In the limit of vanishing ϵ, the requirement of positive $F(\theta, \theta_r, \tilde{h})$ may be simplified to $\theta > \theta_r$.

Substitution of (2.22) and (2.23) into the free-surface kinematic condition, equation (2.15), leads to a nonlinear advection–diffusion equation for $\tilde{h}$ as

$$\frac{\partial \tilde{h}}{\partial \tilde{t}} + \mathscr{C}(\tilde{h}) \frac{\partial \tilde{h}}{\partial \tilde{x}} = \epsilon \frac{\partial}{\partial \tilde{x}} \left[\mathscr{D}(\tilde{h}) \frac{\partial \tilde{h}}{\partial \tilde{x}} \right], \tag{2.24}$$

where

$$\left.\begin{aligned} \mathscr{C}(\tilde{h}) &= \alpha(\theta)\tilde{h}^{3/2} \quad \text{with} \quad \alpha(\theta) = \frac{\sin\theta - \sin\theta_r}{\hat{b}\sqrt{\sin\theta_r}\,\tilde{D}}, \\ \mathscr{D}(\tilde{h}) &= \frac{2}{5}\gamma(\theta)\tilde{h}^{5/2} \quad \text{with} \quad \gamma(\theta) = \frac{\cos\theta}{\hat{b}\sqrt{\sin\theta_r}\,\tilde{D}}. \end{aligned}\right\} \tag{2.25}$$

Such a wave equation has been derived for surface debris flow in a more general conservation form with its solution in Pudasaini (2011) and for water surface flows (Ancey, Cochard & Andreini 2009). An alternative treatment with a nonlinear Burgers equation has also been attempted (Whitham 1974; Borzsonyi *et al.* 2008). In (2.25), both the kinematic wave speed $\mathscr{C}(\tilde{h})$ and the diffusion coefficient $\mathscr{D}(\tilde{h})$ vary nonlinearly with local flow thickness, where the wave speed increases with θ above the repose angle θ_r. The small aspect ratio ϵ in front of the diffusion term makes

it negligible under the general flow condition, as already described in earlier works (Savage & Hutter 1989; Iverson 1997; Gray, Wieland & Hutter 1999; Pudasaini & Hutter 2003; Pudasaini, Wang & Hutter 2005; Pudasaini & Hutter 2007). However, it is shown in § 3 that local dissipation may become important when a shock forms near the front.

The advection–diffusion equation can be solved by the method of characteristic lines as follows:

$$\frac{\mathrm{d}\tilde{h}}{\mathrm{d}\tilde{t}} = \epsilon \frac{\partial}{\partial \tilde{x}} \left[\mathscr{D}(\tilde{h}) \frac{\partial \tilde{h}}{\partial \tilde{x}} \right] \quad \text{along} \quad \frac{\mathrm{d}\tilde{x}}{\mathrm{d}\tilde{t}} = \mathscr{C}(\tilde{h}), \tag{2.26a,b}$$

which specifies the temporal evolution of the surface profile with the diffusive term in a reference moving along the trajectory characteristic lines, $\tilde{x}(\tilde{t})$.

3. Asymptotic solutions for flow dynamics and coherence length

Under the assumption that a static deposit does not modify the shear stress model and hence the predicted flow motion, the same governing equations remain valid for $\tilde{x} > \tilde{x}_d$. Since (2.24) degenerates when $\epsilon \to 0$, the solution is sought by the matched asymptotic method (Hunt 1994; Ancey *et al.* 2009) in terms of an outer and an inner solution that will be distinguished by the subscripts 'o' and 'i' hereinafter.

3.1. *Outer solution*

As $\epsilon \to 0$, equation (2.24) is degenerated into the following nonlinear advection equation,

$$\frac{\partial \tilde{h}_o}{\partial \tilde{t}} + \alpha(\theta) \tilde{h}_o^{3/2} \frac{\partial \tilde{h}_o}{\partial \tilde{x}} = 0, \tag{3.1}$$

which can be transformed into

$$\frac{\mathrm{d}\tilde{h}_o}{\mathrm{d}\tilde{t}} = 0 \quad \text{along} \quad \frac{\mathrm{d}\tilde{x}}{\mathrm{d}\tilde{t}} = \alpha(\theta) \tilde{h}_o^{3/2}. \tag{3.2.a,b}$$

An implicit solution is thus found, $\tilde{h}_o$ being a constant along the characteristic lines, $\tilde{x} = \tilde{x}_0 + \alpha(\theta) \tilde{h}_o^{3/2} \tilde{t}$, with $\tilde{x}_0$ denoting the initiation location. If the mass propagates a sufficiently long distance downstream, the influence of the initial condition is degraded and the leading-order flow surface profile can be approximated by

$$\tilde{h}_o = \left(\frac{\tilde{x} - \tilde{x}_0}{\alpha(\theta)\tilde{t}} \right)^{2/3} \simeq \left(\frac{\tilde{x}}{\alpha(\theta)\tilde{t}} \right)^{2/3} \quad \text{for } \tilde{x} \gg \tilde{x}_0. \tag{3.3}$$

The result is dynamically equivalent to equation (9) in Pudasaini (2011) derived in a more general context. The flow front in the outer solution is located by considering the conservation of total mass, $\tilde{M} = \int_0^{\tilde{x}_{fo}(\tilde{t})} \tilde{h}(\tilde{x}, \tilde{t})\, \mathrm{d}\tilde{x}$, which gives

$$\tilde{x}_{fo}(\tilde{t}) = (\tfrac{5}{3})^{3/5} \alpha(\theta)^{2/5} \tilde{M}^{3/5} \tilde{t}^{2/5}, \tag{3.4}$$

and a front depth, determined by using (3.4) in (3.3), as

$$\tilde{h}_{fo}(\tilde{t}) = (\tfrac{5}{3})^{2/5} \alpha(\theta)^{-2/5} \tilde{M}^{2/5} \tilde{t}^{-2/5}. \tag{3.5}$$

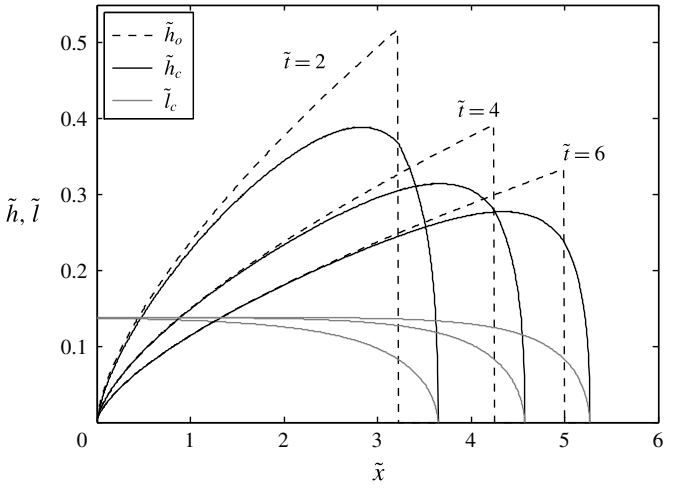

FIGURE 2. Scaled surface profile by the outer solution, $\tilde{h}$, the composite solution, $\tilde{h}_c$, and the composite coherence length, $\tilde{l}_c$, at $\tilde{t}=2$, 4 and 6 ($\theta=23°$, $\theta_r=21°$, $\epsilon=0.1$, $\tilde{D}=0.01$).

A bulk flow down an incline at $\theta=23°$ with $\epsilon=0.1$ and $\tilde{D}=0.01$, $\tilde{h}_o(\tilde{x},\tilde{t})$ at $\tilde{t}=2$, 4 and 6 is plotted by the dashed line in figure 2. It shows monotonic growth with $\tilde{x}$ and a shock-like front where $\tilde{h}_0$ drops abruptly to zero to generate an unrealistically high slope gradient. A similar height drop at the front has also been reported for more general flow settings in Pudasaini (2011) that later smoothed out by further considering the diffusion term that produced more realistic solutions.

3.2. *Inner solution and the composite surface profile*

According to the matched asymptotic method, the inner solution is sought on a stretched coordinate system moving with $\tilde{x}_{fo}(\tilde{t})$ as sketched in figure 3(*a*). The dimensionless inner variables are denoted by a subscript i as

$$\tilde{x}_i=\frac{\tilde{x}-\tilde{x}_{fo}(\tilde{t})}{\epsilon} \quad \text{and} \quad \tilde{h}_i=\tilde{h}. \tag{3.6a,b}$$

The advection–diffusion equation (2.24) in terms of the inner variables becomes

$$\epsilon\frac{\partial\tilde{h}_i}{\partial\tilde{t}}+[\alpha(\theta)\tilde{h}_i^{3/2}-\dot{\tilde{x}}_{fo}(\tilde{t})]\frac{\partial\tilde{h}_i}{\partial\tilde{x}_i}=\frac{2}{5}\frac{\partial}{\partial\tilde{x}_i}\left(\gamma(\theta)\tilde{h}_i^{5/2}\frac{\partial\tilde{h}_i}{\partial\tilde{x}_i}\right), \tag{3.7}$$

which appears quasi-steady on the moving reference frame to the leading order as $\epsilon\to 0$. Integration with respect to $\tilde{x}_i$ leads to

$$\left\{\frac{2}{5}\left[\alpha(\theta)-\gamma(\theta)\frac{\partial\tilde{h}_i}{\partial\tilde{x}_i}\right]\tilde{h}_i^{3/2}-\dot{\tilde{x}}_{fo}(\tilde{t})\right\}\tilde{h}_i=G(\tilde{t}), \tag{3.8}$$

for which $G(\tilde{t})=0$ is required to ensure a vanished flow height at the front. Excluding the trivial solution of $\tilde{h}_i=0$, we obtain $(2/5)[\alpha(\theta)-\partial\tilde{h}_i/\partial\tilde{x}_i]\tilde{h}^{3/2}-\dot{\tilde{x}}_{fo}(\tilde{t})=0$.

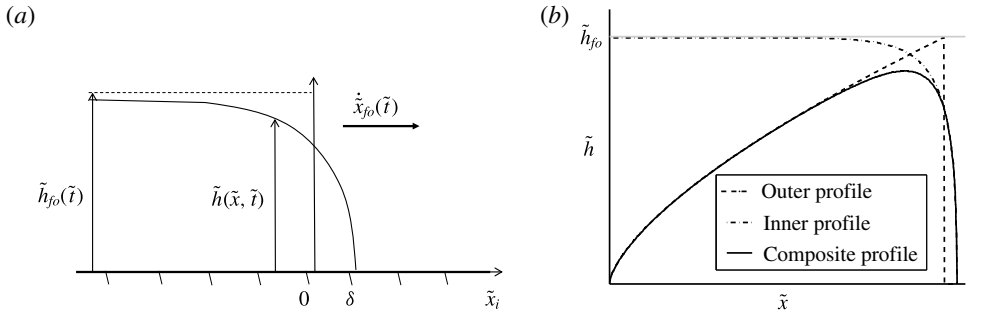

FIGURE 3. (*a*) Schematic diagram of the inner coordinate system and the inner free-surface profile. (*b*) The illustration of the outer, inner and composite free-surface profiles ($\theta = 25°$, $\tilde{t} = 2$, $\theta_r = 21°$, $\epsilon = 0.1$, $\tilde{D} = 0.01$).

If expressing $\dot{\tilde{x}}_{fo}(t)$ in terms of $\tilde{h}_{fo}(\tilde{t})$ by (3.4) and (3.5), we obtain

$$\frac{\partial \tilde{h}_i}{\partial \tilde{x}_i} = \frac{\alpha(\theta)}{\gamma(\theta)}\left[1 - \left(\frac{\tilde{h}_{fo}(\tilde{t})}{\tilde{h}_i}\right)^{3/2}\right]. \tag{3.9}$$

Another integration of (3.9) with respect to the stretched coordinate yields an implicit solution for the inner flow surface profile, with $Z = \tilde{h}_i/\tilde{h}_{fo}(\tilde{t})$ and $X = \tilde{x}_i/\tilde{h}_{fo}(\tilde{t})$, as

$$Z + \frac{2}{\sqrt{3}}\arctan\left(\frac{1+2\sqrt{Z}}{\sqrt{3}}\right) + \frac{1}{3}\ln\left[\frac{(1-\sqrt{Z})^2}{1+\sqrt{Z}+Z}\right] = \frac{\alpha(\theta)}{\gamma(\theta)}X + C_0. \tag{3.10}$$

The integration constant C_0 is determined by the mass redistribution condition with respect to $\tilde{x}_i = 0$ (Huang & Garcia 1998) as

$$\int_{-\infty}^{0} (\tilde{h}_{fo} - \tilde{h}_i)\,\mathrm{d}\tilde{x}_i = \int_0^{\delta} \tilde{h}_i\,\mathrm{d}\tilde{x}_i, \tag{3.11}$$

where δ denotes the displaced inner flow front as marked in figure 3(*a*). By changing the integration variable from $\tilde{h}_i(\tilde{x}_i, \tilde{t})$ to $\tilde{x}_i(\tilde{h}_i, \tilde{t})$, equation (3.11) becomes $\int_0^{\tilde{h}_{fo}(\tilde{t})} \tilde{x}_i\,\mathrm{d}\tilde{h}_i = 0$ or, equivalently, $\int_0^1 X(Z)\,\mathrm{d}Z = 0$, which determines $C_0 = -3/2 + \pi/\sqrt{3}$.

Next, a composite solution is constructed by patching the outer and the inner solutions and then removing their overlap. From (3.11), it is straightforward to show that the inner solution asymptotes to $\tilde{h}_{fo}(\tilde{t})$, so that it automatically matches the outer solution,

$$\lim_{\tilde{x}_i \to -\infty} \tilde{h}_i = \lim_{\tilde{x} \to \tilde{x}_{fo}(\tilde{t})} \tilde{h} = \tilde{h}_{fo}(\tilde{t}). \tag{3.12}$$

Hence, their overlap is simply $\tilde{h}_{fo}(\tilde{t})$ and the final composite solution, denoted by a subscript 'c', is found as

$$\tilde{h}_c(\tilde{x}, \tilde{t}) = \tilde{h}_o(\tilde{x}, \tilde{t}) + \tilde{h}_i(\tilde{x}, \tilde{t}) - \tilde{h}_{fo}(\tilde{t}), \tag{3.13}$$

as illustrated for a typical flow case in figure 3(*b*). The composite surface profile exhibits smoother variation across the spreading length than the outer solution.

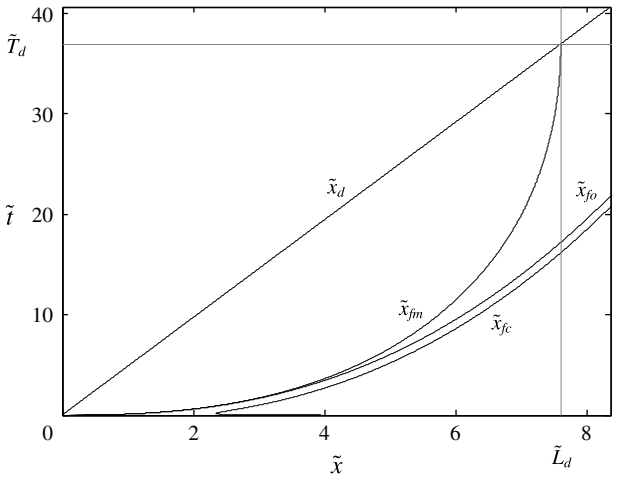

FIGURE 4. Comparison of the scaled flow-front trajectory by the outer, composite and modified solutions as $\tilde{x}_f$, $\tilde{x}_{fc}$ and $\tilde{x}_{fm}$, respectively. The deposit-front trajectory, $\tilde{x}_d$, is also shown with the run-out, $\tilde{L}_d$, and the arrest time, $\tilde{T}_d$, marked ($\theta = 23°$, $\theta_r = 21°$, $\epsilon = 0.1$, $\tilde{D} = 0.01$).

The modified flow-front composite trajectory is determined by adding the shifted inner flow front to the outer solution as $\tilde{x}_{fc}(\tilde{t}) = \tilde{x}_{fo}(\tilde{t}) + \epsilon\delta$, with δ being determined specifically by where the inner flow surface diminishes smoothly to zero, $\delta = \tilde{x}_i(\tilde{h}_i = 0)$, to obtain

$$\tilde{x}_{fc}(\tilde{t}) = \left(\frac{5}{3}\right)^{3/5} \alpha(\theta)^{2/5}\tilde{t}^{2/5} + \epsilon\left(\frac{3}{2} + \frac{2\pi}{3\sqrt{3}}\right)\left(\frac{5}{3}\right)^{2/5} \alpha(\theta)^{-7/5}\gamma(\theta)\tilde{t}^{-2/5}. \tag{3.14}$$

The composite solution for the front trajectory is compared to the outer solution in figure 4 for the motion studied in figure 2. The composite front $\tilde{x}_{fc}(\tilde{t})$ is found to advance $\tilde{x}_{fo}(\tilde{t})$ at a seemingly too drastic manner at small times due to the diverging nature of $\delta \sim \tilde{t}^{-2/5}$ when $\tilde{t} \to 0$. Such a singularity is inevitable since the assumption of $\epsilon \ll 1$ is seldom met shortly after the onset of motion and is degraded when the mass propagates into a shallow configuration at later times.

3.3. *Local coherence length and flow regimes*

The composite flow solution is now employed to investigate how the coherence length, l, develops with the flow. In the limit of $\epsilon \to 0$, equations (2.19) and (2.21) give

$$\tilde{l}_o = \frac{\sin\theta_r\, \hat{b}\tilde{D}}{\sin\theta - \sin\theta_r}, \tag{3.15}$$

which is the outer solution of the coherence length valid for $\tilde{x} \ll \tilde{x}_f(\tilde{t})$. When $\tilde{x} \sim \tilde{x}_f(\tilde{t})$, equation (2.19) gives $\tilde{l}_i = \sin\theta_r\, \hat{b}\tilde{D}(\sin\theta - \cos\theta\, \partial\tilde{h}_i/\partial\tilde{x}_i - \sin\theta_r)^{-1}$ in the inner coordinate system and the local $\partial\tilde{h}_i/\partial\tilde{x}_i$ can be replaced by (3.9) to give

$$\tilde{l}_i = \frac{\sqrt{\sin\theta_r}}{\alpha(\theta)}\left(\frac{\tilde{h}_i}{\tilde{h}_{fo}}\right)^{3/2}. \tag{3.16}$$

It is straightforward to show that the inner coherence length asymptotes to the outer solution, $\lim_{\tilde{x}_i\to-\infty}\tilde{l}_i=\tilde{l}_o$, so that the overlap solution is, again, the outer solution and the composite solution can be found readily as $\tilde{l}_c=\tilde{l}_o+\tilde{l}_i-\tilde{l}_o=\tilde{l}_i$. By expressing (3.16) in terms of $\tilde{l}_o$, we obtain

$$\tilde{l}_c=Z^{3/2}\tilde{l}_o, \tag{3.17}$$

clearly showing that the profile of $\tilde{l}_c$ is governed by the implicit solution of $Z=\tilde{h}_i/\tilde{h}_{fo}$ from (3.10) near the front but asymptotes to constant $\tilde{l}_o$ when $\tilde{x}\ll\tilde{x}_f(\tilde{t})$. When the instantaneous coherence length profile for the flow cases examined in figure 2 are shown by the solid grey lines on the same plot, $\tilde{l}_c(\tilde{x},\,\tilde{t})$ is found to increase monotonically from zero at the flow front onto a plateau of $\tilde{l}_o$ in the rear.

The relative magnitude of $\tilde{l}_c(\tilde{x},\,\tilde{t})$ and $\tilde{h}_c(\tilde{x},\,\tilde{t})$ can be utilized to categorize bulk motion into different regimes as follows. When $\tilde{h}_c\gg\tilde{l}_c$ in the front, the majority of the material is in the flowing state and the diminished $\tilde{l}_c$ at the front signals free and agitated grain motions therein, which agrees qualitatively with the experimental observations at a surging front (Pouliquen & Forterre 2002; Kokelaar *et al.* 2014). When $\tilde{l}_c$ grows comparable to $\tilde{h}_c$ in the rear, effective spatial correlation across the layer develops to transmit the bulk-arresting decelerating impulse due to basal friction, so that the deposit develops from the base as shown by Pudasaini (2011). Such a fluid-to-solid transition first takes place in the rear where $\tilde{h}_c(\tilde{t})\sim\tilde{l}_c$ and propagates towards the front as $\tilde{h}_c$ diminishes when the mass evolves downstream (see figure 1). Such a deposition wave phenomenon has been observed in experiments (Borzsonyi *et al.* 2008; Edwards & Gray 2014).

4. Propagation of the deposit front and the arrested state

4.1. *Leading-order solutions*

As stated in § 3, the current model assumes that a static deposit develops from the base when $\tilde{l}$ becomes comparable to $\tilde{h}$ at $\tilde{x}_d$. Hence, the flow solutions remain unaffected for $\tilde{x}>\tilde{x}_d$ and the local flow height as well as the propagation speed of the deposition front at $\tilde{x}_d$ can be described by (2.26) as

$$\frac{\mathrm{d}\tilde{h}_d}{\mathrm{d}\tilde{t}}=\epsilon\,\frac{\partial}{\partial\tilde{x}}\left[\frac{2}{5}\gamma(\theta)\tilde{h}^{5/2}\frac{\partial\tilde{h}}{\partial\tilde{x}}\right]\Bigg|_{\tilde{x}=\tilde{x}_d(\tilde{t})}, \tag{4.1}$$

$$\dot{\tilde{x}}_d(\tilde{t})=\alpha(\theta)\tilde{h}_d^{3/2}(\tilde{t}), \tag{4.2}$$

assuming that $\tilde{x}_d$ is known *a priori*. Hence, we follow Ertas & Halsey (2002) to determine an instantaneous $\tilde{x}_d(\tilde{t})$ by

$$\tilde{h}_d(\tilde{t})=\hat{c}\tilde{l}(\tilde{x}_d(\tilde{t}),\,\tilde{t}). \tag{4.3}$$

Here, the coefficient constant $\hat{c}$ is set to the value in the dimensional relation $h_{stop}(\theta)=\hat{c}l(\theta)$ used by Ertas & Halsey (2002) to specify the relationship between the coherence length in a uniform surface flow and the thickness threshold h_{stop}. This is because the two relations in uniform steady and non-uniform unsteady flows are conceptually equivalent and only differ in how the flow-to-no-flow transition develops with the flow. For steady flows of uniform thickness, the transition takes place immediately

across the layer and the flow stops *en masse*. When the bulk surface is non-uniform and changes with time, a static layer can develop gradually from the bed to the free surface although in a manner yet unresolved from the current model. That is why the solid–fluid interface is sketched schematically by both a concave and another convex dashed line in figure 1 to show its undetermined nature. Nonetheless, a leading-order estimation of the total mass run-out and arrest time can still be attempted using the assumed unaffected flow solutions above the just-formed deposit at $\tilde{x} = \tilde{x}_d$ as follows.

Firstly, an arrest time, $\tilde{T}_d$, for the total mass to halt can be estimated by requiring total mass conservation,

$$\tilde{M} = \int_0^{\tilde{T}_d} \dot{\tilde{x}}_d(\tilde{t})\tilde{h}_d(\tilde{t})\,\mathrm{d}\tilde{t}, \tag{4.4}$$

where $\dot{\tilde{x}}_d(\tilde{t})\tilde{h}_d(\tilde{t})$ is the mass flux across a normal plane at $\tilde{x}_d(\tilde{t})$. We now seek the leading-order solution of the above deposit-front model. In the limit of $\epsilon \to 0$, equation (4.1) gives

$$\frac{\mathrm{d}\tilde{h}_d}{\mathrm{d}\tilde{t}} = 0, \tag{4.5}$$

and hence a time-invariant constant may be estimated to the leading order using the outer constant solution in (3.15) as

$$\tilde{h}_d = \hat{c}\tilde{l}_o. \tag{4.6}$$

This in turn gives a constant speed for the deposition front by (4.2). Hence, the integrand in (4.4) is independent of $\tilde{t}$, to the leading order, so that it is straightforward to obtain

$$\tilde{T}_d = \tilde{M}\hat{b}^{-3/2}\hat{c}^{-3/2}\tilde{D}^{-3/2}\sqrt{\sin\theta_r}\,(\sin\theta - \sin\theta_r)^{3/2}. \tag{4.7}$$

With $\dot{\tilde{x}}_d$ and $\tilde{T}_d$, a leading-order estimation of the total run-out distance can be found readily as

$$\tilde{L}_d = \int_0^{\tilde{T}_d} \dot{\tilde{x}}_d(\tilde{t})\,\mathrm{d}\tilde{t} = \tilde{M}\hat{b}^{-1}\tilde{D}^{-1}(\sin\theta - \sin\theta_r). \tag{4.8}$$

4.2. *Modified flow-front solution*

It is apparent that the finite $\tilde{L}_d$ given by (4.8) is inconsistent with the front trajectory profiles found in the outer and the composite solution in (3.4) and (3.14) that give an unstoppable solution and hence an infinite run-out as also found in Pudasaini (2011). The discrepancy is attributed to the assumptions that the solid deposit does not affect the flow solutions. The current stress model may underestimate flow resistance since internal friction at the fluid-to-solid interface is not considered and neither is the possible momentum loss during the deposition process. To construct a more realistic front trajectory profile within the current framework, we try to adapt the asymptotic solution to meet the requirement that the flow front arrests as soon as it travels over $\tilde{L}_d$ at $\tilde{t} = \tilde{T}_d$. For simplicity, such a modification is proposed for the outer solution (3.4) by imposing an *ad hoc* prefactor to generate the modified front trajectory as

$$\tilde{x}_{fm}(\tilde{t}) = \left[1 - \hat{f}\left(\frac{\tilde{t}}{\tilde{T}_d}\right)^{\hat{g}}\right]\tilde{x}_{fo}(\tilde{t}), \tag{4.9}$$

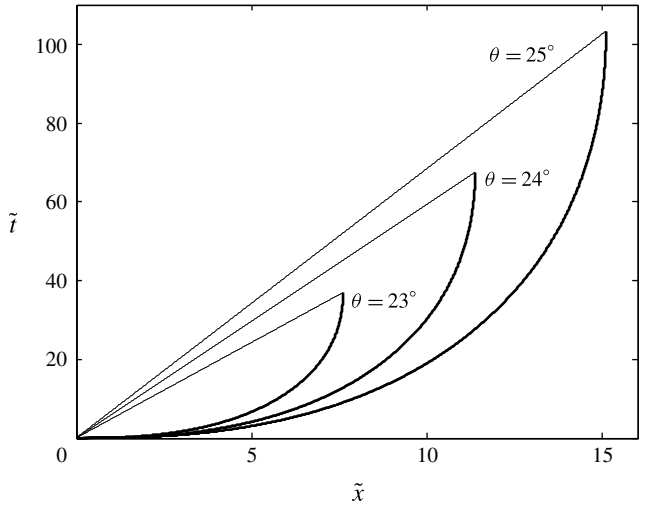

FIGURE 5. Comparison of the modified front trajectory $\tilde{x}_{fm}$ (thick solid line) with $\tilde{x}_d$ (thin solid line) for $\theta = 23^\circ, 24^\circ, 25^\circ$, where $\theta_r = 21^\circ$, $\epsilon = 0.1$, $\tilde{D} = 0.01$.

with two unknown constants $\hat{f}$ and $\hat{g}$. By requiring $\tilde{x}_{fm}(\tilde{T}_d) = \tilde{L}_d$ and $\dot{\tilde{x}}_{fm}(\tilde{T}_d) = 0$, $\hat{f} = 1 - (3/5)^{3/5}$ and $\hat{g} = (2/5)(1-\hat{f})/\hat{f}$. A similar solution may be constructed using the composite front trajectory (3.14), which leads to more complex results. When the modified front trajectory is presented on figure 4, $\tilde{x}_{fm}(\tilde{t})$ is observed to asymptote to $\tilde{x}_{fo}(\tilde{t})$ at early times but decelerate smoothly to the run-out $\tilde{L}_d$ at the intersection of $\tilde{x}_{fm}(\tilde{t})$ and $\tilde{x}_d(\tilde{t})$ at $\tilde{t} = \tilde{T}_d$. The trajectories of $\tilde{x}_{fm}(\tilde{t})$ and $\tilde{x}_d(\tilde{t})$ for flows under different θ are plotted in figure 5, showing longer deposits and arrest time on steeper inclines.

4.3. *Comparison with experimental data*

The current results of the modified flow front in (4.9) and the leading-order arrest time and run-out in (4.7) and (4.8) are evaluated by comparison with the experimental data reported in Pouliquen & Forterre (2002). Those authors studied the spreading of finite glass beads ($D = 0.5$ mm) from spherical caps of different sizes down a rough incline at different inclination angles, and the results for the medium cap are considered here. Since the current analysis is two-dimensional, justification and explanations are given below for how we interpreted the three-dimensional experimental data in the reference.

Judging from figures 5(a), 6 and 7(a) in Pouliquen & Forterre (2002) for the top view of a granular mass down an incline at $\theta = 23^\circ$, the instantaneous flow width in the consecutive snapshots shortly after the release remains nearly constant. The final deposit widths for releases on different slopes are also close to each other. Both observations suggest that the lateral spreading mechanism is rather insensitive to changes in the examined flow conditions and hence is assumed here to be much weaker than streamwise propagation. As a result, the flow can be fairly regarded as quasi-two-dimensional with a total volume per unit width of $M/\rho \simeq 13$ cm^2. This value is estimated here by the projection area of the deposit at $\theta = 23^\circ$ shown in their figure 6(c), which may be overestimated since the transverse surface curvature is neglected. A closer look at the surface contour lines provided therein reveals that such approximation of a quasi-two-dimensional block mass is more feasible at later times.

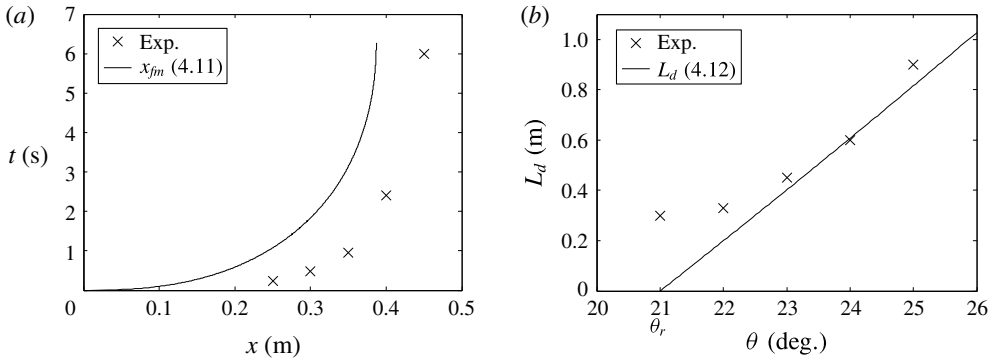

FIGURE 6. Comparison of the current prediction with the experimental data reported in Pouliquen & Forterre (2002): (*a*) front trajectory at $\theta = 23^\circ$ with $x_f = 25$, 30, 35, 40 and 45 cm extracted here for $t = 0.24$, 0.48, 0.96, 2.4 and 6 s. (*b*) Run-out distance under different inclination angles, where $\theta_r = 21^\circ$ is taken to be θ_1 in Pouliquen & Forterre (2002).

However, the effect of the varying degree of an overestimated mass falls beyond the scope of this work and is not further addressed.

As suggested by Ertas & Halsey (2002), bulk material constants are evaluated by comparing the model prediction for uniform flows with Pouliquen's flow rule and h_{stop} in the limit of $\theta \to \theta_r$ to yield

$$\theta_r = \theta_1, \quad \hat{b} = \frac{2\mathscr{L}(\tan\theta_2 - \tan\theta_1)\cos\theta_1}{5\beta\sqrt{\sin\theta_1}\,D}, \quad \hat{c} = \frac{5\beta}{2\sqrt{\sin\theta_1}}, \tag{4.10a–c}$$

where $\beta = 0.136$, $\theta_1 = 21^\circ$, $\theta_2 = 30.7^\circ$, $\mathscr{L} = 0.65$ mm and $D = 0.5$ mm. Equations (4.9), (4.7) and (4.8) are expressed in dimensional forms as

$$x_{fm}(t) = \left(\frac{5}{3}\right)^{3/5}\left(\frac{M}{\rho}\right)^{3/5}\left(\sqrt{\frac{g}{\sin\theta_r}}\frac{\sin\theta - \sin\theta_r}{\hat{b}D}\right)^{2/5}\left[1 - \hat{f}\left(\frac{t}{T_d}\right)^{\hat{g}}\right]t^{2/5}, \tag{4.11a}$$

with

$$T_d(\theta) = \left(\frac{M}{\rho}\right)\sqrt{\frac{\sin\theta_r}{\hat{b}^3\hat{c}^3D^3g}}(\sin\theta - \sin\theta_r)^{3/2} \tag{4.11b}$$

and

$$L_d(\theta) = \left(\frac{M}{\rho}\right)\hat{b}^{-1}D^{-1}(\sin\theta - \sin\theta_r). \tag{4.12}$$

Focusing on the flow-front dynamics at $\theta = 23^\circ$ (in the valid range $\theta_r < \theta < \theta_2$ for the current model), the successive front locations are extracted from figure 5(c) in Ertas & Halsey (2002) and compared to the prediction by (4.11*a*) in figure 6(*a*). Qualitative agreement on the nonlinear front trajectory is observed and the predicted arrest time, $T_d = 6.27$ s, is within a 4.5 % overestimation from the measured 6 s. A shorter L_d is therefore predicted throughout the process, which may further result from the following reasons. First, the *ad hoc* modification is constructed on the outer solution for order consistency and hence does not incorporate the inner flow-front

advancement by δ in (3.14). Further, the current flow solution neglects the influence of the initial boundary condition on the characteristic line in the derivation of $\tilde{h}_o$ in (3.3). Inclusion of $\tilde{x}_0$ therein should give a greater $\tilde{x}_{fo}(\tilde{t})$ and hence L_d to reflect the influence of initial packing shape, especially on the slower motion near θ_r with shorter run-outs. Finally, the run-outs on different slopes reported in figure 7(b) of Ertas & Halsey (2002) and from the current predictions are also compared in figure 6(*b*), showing satisfactory agreement when $\theta > 23^\circ$. The growing degree of underestimation when $\theta \to \theta_r$ clearly illustrates the limitation of the current shear stress model in (1.2) and is further discussed in § 5.

5. Summary and discussion

The coherence length model of shear stress and the arresting mechanism proposed by Ertas & Halsey (2002) for steady uniform granular flows down a rough inclined surface are adopted to theoretically solve the propagation dynamics of a finite dry granular mass in a shallow configuration down an incline. The analysis focuses on the dynamics in long run-outs so that the influences of initial packing shape and bulk inertia are both neglected. The free-surface height, $h(x, t)$, is governed by a nonlinear advection–diffusion equation for which the matched asymptotic solution is derived with respect to a small height-to-length aspect ratio. The solutions are used to determine the flow-front trajectory under a total mass conservation condition. The streamwise velocity component shows a Bagnold-like depth profile with a magnitude varying with the net driving force after the gravity component along the incline is balanced by internal resistance and the normal pressure force induced by $\partial h/\partial x$. Variation of surface flow height further induces a non-zero normal velocity. According to Ertas & Halsey (2002), the arresting impulse acts across a coherence length scale $l(x, t)$ that varies with $h(x, t)$ and is found to grow from zero at the flow front to a constant. It is then postulated that the local flow is arrested when $h_d(x, t) = \hat{c} l_o(x, t)$, with $\hat{c}$ evaluated from uniform flow dynamics, and the deposit front, $x_d(t)$, is determined and found to propagate in time towards the flow front when the finite mass spreads in time into thinner shapes. However, since we assume that a solid deposit has a negligible decelerating effect on the flow solution obtained when it is applied to derive a front trajectory profile, the $x_f(t)$ obtained is overestimated. Modification into $x_{fm}(t)$ is proposed using the outer solutions so that it meets $x_d(t)$ when the entire running mass is brought to a halt at the finite arrest time T_d. With the modified model, the predictions of the transient front trajectory and the run-out distance show satisfactory agreement with the measurements in Pouliquen & Forterre (2002) for $\theta > 23^\circ$.

It should be noted that the present analysis is valid for $\theta_r < \theta < \theta_2$. When $\theta > \theta_2$, the coherence length is degraded to approximately one particle diameter and the flow can accelerate downstream as mentioned in § 1, invalidating the inertia-free kinematic wave equation in (2.18), which necessitates a fast velocity scaling to preserve the full x-momentum equation. On the other hand, when θ decreases to approximately θ_1, the model prediction underestimates the experimental data as shown in figure 6(*b*) to give a zero velocity and run-out right at θ_r. This latter phenomenon shows that no flow is possible for $\theta < \theta_r$, which contradicts the common observation that an avalanche can occur on any slope. This discrepancy results from the fact that the shear stress model (1.2) only accounts for the long-range collisional momentum transfer across the length scale $l_v(l, D)$. When l_v, or equivalently the coherence length, approaches h, the direct and hence more effective pathway to transmit decelerating impulse through contacting

grains is not taken into account in the current formulation. This also explains why the current analysis cannot provide an unsteady fluid-to-solid transition process for $x < x_d(t)$, which requires a more refined stress model that addresses the effects of flow thickness through a rate- and pressure-dependent Coulomb–viscoplastic model (Domnik & Pudasaini 2012; Domnik *et al.* 2013) or size-dependent boundary effect that is also known as the non-local effect (GDRMidi 2004; Aranson *et al.* 2008; Pouliquen & Forterre 2009; Staron *et al.* 2010; Reddy, Forterre & Pouliquen 2011; Kamrin & Koval 2012; Bouzid *et al.* 2013). There is also a different approach that directly accounts for the transient configuration of force chains and their interaction with the ambient flow in formulating bulk shear stress (Mills, Loggia & Tixier 1999).

Although the numerical solution of the depth-averaged model by Pouliquen & Forterre (2002) can capture actual run-outs over a range of slope angles close to the angle of repose, the current analysis provides an explicit formula with fair accuracy while suggesting two distinct deposition mechanisms in view of the flow height scale H and the maximum coherence length $l_o(\theta)$ in (3.15). When $H/l_o(\theta) \gg 1$ often at $\theta > \theta_r$, the deposition process appears as consecutive jamming of weakly correlated structure. In contrast, when $H/l_o(\theta) \sim 1$ at $\theta > \theta_r$ or when $l_o(\theta)$ diverges at $\theta \leqslant \theta_r$, an avalanche may be interpreted as a local event on steeper internal structure formed by the strongly correlated grain motions near the base. It will be an interesting extension to incorporate size dependence or boundary effect into the coherence length model in both the stress formulation and the arresting mechanism. However, it is likely that the governing equations obtained would require numerical solutions like most studies in the literature.

Acknowledgement

This project was supported by the Ministry of Science and Technology of Taiwan through the grant 103-2221-E-002-174-MY2.

Appendix A. Derivation of equations (2.19) and (2.20)

Integration of (2.18) with respect to $\tilde{y}$ with the boundary condition in (2.14) gives the shear stress profile across the depth as

$$\tilde{\sigma}_{yx} = \left(\sin\theta - \epsilon\cos\theta\frac{\partial\tilde{h}}{\partial\tilde{x}}\right)(\tilde{h}-\tilde{y}). \tag{A 1}$$

By eliminating $\tilde{l}_v$ using (2.12) and (2.13), we obtain

$$\tilde{\sigma}_{yx} = \tilde{l}^2\left(1+\hat{b}\frac{\tilde{D}}{\tilde{l}}\right)\left(\frac{\partial\tilde{u}}{\partial\tilde{y}}\right)^2. \tag{A 2}$$

When (A 2) is employed to express $\partial\tilde{u}/\partial\tilde{y}$ in terms of $\tilde{l}$, equation (2.11) can be rewritten as

$$\tilde{l}^2\left|\frac{\partial}{\partial\tilde{y}}\left(\frac{\tilde{\sigma}_{yx}}{\tilde{l}^2+\hat{b}\tilde{D}\tilde{l}}\right)\right| = \hat{a}f(e). \tag{A 3}$$

Equation (A 1) is then substituted into (A 3) to find the equation for $\tilde{l}$ and $\tilde{y}$ as

$$\frac{2\tilde{l}+R}{(S-A)\tilde{l}^2+(S-2A)R\tilde{l}-AB^2}\frac{\partial\tilde{l}}{\partial\tilde{y}} = S^{-1}(\tilde{h}-\tilde{y})^{-1}, \tag{A 4}$$

with

$$S = \sin\theta - \epsilon\cos\theta\frac{\partial\tilde{h}}{\partial\tilde{x}} > 0, \quad A = \hat{a}f(e) \quad \text{and} \quad R = \hat{b}\tilde{D}. \tag{A 5a–c}$$

Equation (A 4) is then integrated with respect to $\tilde{y}$ to give

$$(\tilde{l}+R)[(S-A)\tilde{l}-AR]^{(S+A/S-A)}(\tilde{h}-\tilde{y}) = C, \tag{A 6}$$

for which we determine $C = C(\tilde{x},\tilde{t}) = 0$ by requiring $\tilde{y} = \tilde{h}$. Since $\tilde{l} \geqslant 0$, the terms within the square brackets must vanish in (A 6) so that $\tilde{l} = AR/(S-A)$, or

$$\tilde{l} = \frac{\hat{a}f(e)\hat{b}\tilde{D}}{\sin\theta - \epsilon\cos\theta\,\partial\tilde{h}/\partial\tilde{x} - \hat{a}f(e)}. \tag{A 7}$$

Substitution of (A 1) and (A 7) to (A 2) returns the shear rate in (2.20) after some straightforward manipulations.

REFERENCES

ANCEY, C., COCHARD, S. & ANDREINI, N. 2009 The dam-break problem for viscous fluids in the high-capillary-number limit. *J. Fluid Mech.* **624**, 1–22.

ANDREOTTI, B., FORTERRE, Y. & POULIQUEN, O. 2013 *Granular Media: Between Fluid and Solid*. Cambridge University Press.

ARANSON, I. S. & TSIMRING, L. S. 2002 Continuum theory of partially fluidized granular flows. *Phys. Rev.* E **65**, 061303.

ARANSON, I. S., TSIMRING, L. S., MALLOGGI, F. & CLÉMENT, E. 2008 Nonlocal rheological properties of granular flows near a jamming limit. *Phys. Rev.* E **78**, 031303.

BAGNOLD, R. A. 1954 Experiments on a gravity-free dispersion of large solid spheres in a Newtonian fluid under shear. *Proc. R. Soc. Lond.* A **225** (1160), 49–63.

BALMFORTH, N. J. & KERSWELL, R. R. 2005 Granular collapse in two dimensions. *J. Fluid Mech.* **538**, 399–428.

BARAN, O., ERTAŞ, D., HALSEY, T. C., GREST, G. S. & LECHMAN, J. B. 2006 Velocity correlations in dense gravity-driven granular chute flow. *Phys. Rev.* E **74**, 051302.

BORZSONYI, T., HALSEY, T. C. & ECKE, R. E. 2008 Avalanche dynamics on a rough inclined plane. *Phys. Rev.* E **78**, 011306.

BOUCHAUD, J. P., CATES, M., PRAKASH, J. R. & EDWARDS, S. F. 1994 A model for the dynamics of sandpile surfaces. *J. Phys. (Paris)* I **4**, 1383–1410.

BOUTREUX, T., RAPHAEL, E. & DE GENNES, P. G. 1998 Surface flows of granular materials: a modified picture for thick avalanches. *Phys. Rev.* E **58**, 4692–4700.

BOUZID, M., TRULSSON, M., CLAUDIN, P., CLÉMENT, E. & ANDREOTTI, B. 2013 Nonlocal rheology of granular flows across yield conditions. *Phys. Rev. Lett.* **111**, 238301.

DAERR, A. 2001 Dynamical equilibrium of avalanches on a rough plane. *Phys. Fluids* **13**, 2115–2124.

DAERR, A. & DOUADY, S. 1999 Two types of avalanche behaviour in granular media. *Nature* **399**, 241–243.

DOMNIK, B. & PUDASAINI, S. P. 2012 Full two-dimensional rapid chute flows of simple viscoplastic granular materials with pressure-dependent dynamic slip-velocity and their numerical simulations. *J. Non-Newtonian Fluid Mech.* **173**, 72–86.

DOMNIK, B., PUDASAINI, S. P., KATZENBACH, R. & MILLER, S. A. 2013 Coupling of full two-dimensional and depth-averaged models for granular flows. *J. Non-Newtonian Fluid Mech.* **201**, 56–68.

EDWARDS, A. N. & GRAY, J. M. N. T. 2014 Erosion–deposition waves in shallow granular free-surface flows. *J. Fluid Mech.* **762**, 35–37.

ERTAS, D. & HALSEY, T. C. 2002 Granular gravitational collapse and chute flow. *Eur. Phys. Lett.* **60**, 931–937.

GDRMIDI 2004 On dense granular flows. *Eur. Phys. J.* E **14**, 341–365.

GRAY, J. M. N. T. & ANCEY, C. 2009 Segregation, recirculation and deposition of coarse particles near two-dimensional avalanche fronts. *J. Fluid Mech.* **629**, 387–423.

GRAY, J. M. N. T. & EDWARDS, A. N. 2014 A depth-averaged $\mu(I)$-rheology for shallow granular free-surface flows. *J. Fluid Mech.* **755**, 503–534.

GRAY, J. M. N. T., WIELAND, M. & HUTTER, K. 1999 Gravity-driven free surface flow of granular avalanches over complex basal topography. *Phil. Trans. R. Soc. Lond.* A **455** (1985), 1841–1874.

HOGG, A. J. 2007 Two dimensional granular slumps down slopes. *Phys. Fluids* **19**, 093301.

HUANG, X. & GARCIA, M. H. 1998 A Herschel–Bulkley model for mud flow down a slope. *J. Fluid Mech.* **374**, 305–333.

HUNT, B. 1994 Newtonian fluid mechanics treatment of debris flows and avalanches. *J. Hydraul. Engng ASCE* **120**, 1350–1363.

IVERSON, R. M. 1997 The physics of debris flows. *Rev. Geophys.* **35** (3), 245–296.

JENKINS, J. T. 2006 Dense shearing flows of inelastic disks. *Phys. Fluids* **18**, 103307.

KAMRIN, K. & HENANN, D. 2015 Modeling the nonlocal behavior of granular flows down inclines. *Soft Matt.* **11**, 179–185.

KAMRIN, K. & KOVAL, G. 2012 Nonlocal constitutive relation for steady granular flow. *Phys. Rev. Lett.* **108**, 178301.

KOKELAAR, B. P., GRAHAM, R. L., GRAY, J. M. N. T. & VALLANCE, J. W. 2014 Fine-grained linings of leveed channels facilitate runout of granular flows. *Earth Planet. Sci. Lett.* **385**, 172–180.

KUMARAN, V. 2008 Dense granular flow down an inclined plane: from kinetic theory to granular dynamics. *J. Fluid Mech.* **599**, 121–168.

LOUGE, M. Y. 2003 Model for dense granular flows down bumpy inclines. *Phys. Rev.* E **67**, 061303.

MANGENEY-CASTELNAU, A., BOUCHUT, F., VILOTTE, J. P., LAJEUNESSE, E., AUBERTIN, A. & PIRULLI, M. 2005 On the use of Saint Venant equations to simulate the spreading of a granular mass. *J. Geophys. Res.* **110** (B9), B09103.

MANGENEY-CASTELNAU, A., ROCHE, O., HUNGR, O., MANGOLD, N., FACCANONI, G. & LUCAS, A. 2010 Erosion and mobility in granular collapse over sloping beds. *J. Geophys. Res.* **115** (F3), F03040.

MILLS, P., LOGGIA, D. & TIXIER, M. 1999 Model for a stationary dense granular flow along an inclined wall. *Eur. Phys. Lett.* **45**, 733–738.

POULIQUEN, O. 1999 Scaling laws in granular flows down rough inclined planes. *Phys. Fluids* **11**, 542–548.

POULIQUEN, O. 2004 Velocity correlations in dense granular flows. *Phys. Rev. Lett.* **93**, 248001.

POULIQUEN, O. & FORTERRE, Y. 2002 Friction law for dense granular flows: application to the motion of a mass down a rough inclined plane. *J. Fluid Mech.* **453**, 133–151.

POULIQUEN, O. & FORTERRE, Y. 2009 A non-local rheology for dense granular flows. *Phil. Trans. R. Soc. Lond.* A **367**, 5091–5107.

PUDASAINI, S. P. 2011 Some exact solutions for debris and avalanche flows. *Phys. Fluids* **23**, 043301.

PUDASAINI, S. P. & HUTTER, K. 2003 Rapid shear flows of dry granular masses down curved and twisted channels. *J. Fluid Mech.* **495**, 193–208.

PUDASAINI, S. P. & HUTTER, K. 2007 *Avalanche Dynamics, Dynamics of Rapid Flows of Dense Granular Avalanches*. Springer.

PUDASAINI, S. P., WANG, Y. & HUTTER, K. 2005 Modelling debris flows down general channels. *Nat. Hazards Earth Syst. Sci.* **5** (6), 799–819.

REDDY, K. A., FORTERRE, Y. & POULIQUEN, O. 2011 Evidence of mechanically activated processes in slow granular flows. *Phys. Rev. Lett.* **106**, 108301.

SAVAGE, S. B. & HUTTER, K. 1989 The motion of a finite mass of granular material down a rough incline. *J. Fluid Mech.* **374**, 305–333.

SILBERT, L., LANDRY, J. & GREST, G. 2003 Granular flow down a rough inclined plane: transition between thin and thick piles. *Phys. Fluids* **15**, 1–10.

STARON, L. 2008 Correlated motion in the bulk of dense granular flows. *Phys. Rev.* E **77**, 051304.

STARON, L., LAGRE, P.-Y., JOSSERAND, C. & LHUILLIER, D. 2010 Flow and jamming of a two-dimensional granular bed: toward a nonlocal rheology? *Phys. Fluids* **22** (11), 113303.

TAI, Y. & KUO, C. Y. 2008 A new model of granular flows over general topography with erosion and deposition. *Acta Mechanica* **199**, 71–96.

WHITHAM, G. B. 1974 *Linear and Nonlinear Waves*. Wiley.